Journal of Luminescence 269 (2024) 120520

Contents lists available at ScienceDirect

Journal of Luminescence

journal homepage: www.elsevier.com/locate/jlumin

Full Length Article

In-band luminescence thermometry in the third biological window and multicolor emission of Er-doped fluoride and oxide nanoparticles

F. Gennari [a,*], J. Periša [b], M. Sekulić [b], Ž. Antić [b], M. Dramićanin [b], A. Toncelli [a,c,d]

[a] Dipartimento di Fisica "E. Fermi", Università di Pisa, Largo B. Pontecorvo 3, 56127, Pisa, Italy
[b] Center of Excellence for Photoconversion, Vinča Institute of Nuclear Sciences – National Institute of the Republic of Serbia, University of Belgrade, Serbia
[c] Istituto Nazionale di Fisica Nucleare, Sezione di Pisa, Largo B. Pontecorvo 3, 56127, Pisa, Italy
[d] Centro per l'Integrazione della Strumentazione dell'Università di Pisa (CISUP), Lungarno Pacinotti 43/44, 56126, Pisa, Italy

ARTICLE INFO

Keywords:
Sesquioxide nanoparticles
Flouride nanoparticles
Eribum
LIR
Third biological window

ABSTRACT

In this study we present a morphological and spectroscopical characterization of three different erbium doped nanocrystal samples, namely two oxides (Y_2O_3:3%Er, Sc_2O_3:3%Er) and one fluoride (YF_3:5%Er). The spectroscopic study offers a comprehensive comparison of their multicolor emissions, ranging from the visible to the mid-infrared region. Emissions from the first five excited states are presented and the emission cross sections of the $^4I_{11/2} \rightarrow {}^4I_{15/2}$, $^4I_{11/2} \rightarrow {}^4I_{13/2}$, and $^4I_{13/2} \rightarrow {}^4I_{15/2}$ transitions have been calculated and compared with literature results for the oxide compounds providing a confirmation for the 1.5 μm emission of Er:Y_2O_3, a correction over published values for the 2.7 μm emission of Er:Y_2O_3, and also new results for the Er:Sc_2O_3 emission cross section values of all the infrared bands. Moreover, this study explores the application of the $^4I_{13/2}$ emission for in-band luminescence thermometry within the third biological window. An optimized segmentation of the 1.5 μm emission permits to achieve high relative and absolute sensitivities using just one dopant ion.

1. Introduction

Er-doped nanoparticles of various compositions are generally studied for their visible upconversion fluorescence properties under laser pumping. Er also possesses many visible levels that can be directly excited with low-cost LED pump sources and can give rise to intense visible emission that has already been widely exploited for luminescence intensity ratio (LIR) thermometry applications with good results. Er ions also show many infrared (IR) energy levels that have been used for infrared lasers, for example in the 1.6 μm telecommunication window or in the 2.8 μm mid-infrared region (MIR). Moreover, the near-infrared emission of Er ions at around 1.6 μm almost completely lies in the third biological window and can be exploited for LIR thermometry, although this emission has been less widely studied than the visible one for this purpose until to date [1–6]. In these cases [4–6], the various compounds have been studied in a wide temperature range and the characterization has also been performed in organic and aqueous solutions with good results, therefore, it is worth investigating other compounds for the same purpose.

Sesquioxide and fluoride materials are generally considered good host crystals for mid-infrared emissions because of their relatively low phonon energy and good thermomechanical properties when grown as bulk materials. In both cases, the bulk crystal growth of these materials is challenging because sesquioxides grow at very high temperatures (around 2400 °C) [7] and fluorides need a very careful control of the growth atmosphere to avoid oxygen contamination which is strongly detrimental for the emission efficiency [8].

Nanoparticle preparation, instead, usually requires low temperatures and it is less critical, cheaper, and less time-consuming. Moreover, nanosized materials exhibit peculiar properties that has opened new perspectives in many applications especially in the biomedical field such as biomedical imaging, nanothermometry or sensing [9].

The preparation of Yttrium Oxide nanoparticles has also been studied for applications in amplification devices operating in telecommunication spectral range [10] both using erbium as single dopant agent or together with other dopants to optimize population inversion and pumping efficiency. Other studies [11,12] focus their attention on Y_2O_3 nano-powder in ceramics or in nanospheres for possible laser applications. Moreover, Erbium–Holmium codoped Y_2O_3 nanoparticles have already been proposed for nano-thermometry [3] with the luminescence intensity ratio calculated between the $^5I_6 \rightarrow {}^5I_8$ and $^4I_{13/2} \rightarrow {}^4I_{15/2}$ emission transitions of Ho and Er, respectively.

* Corresponding author.
E-mail address: fulvia.gennari@phd.unipi.it (F. Gennari).

https://doi.org/10.1016/j.jlumin.2024.120520
Received 16 October 2023; Received in revised form 24 January 2024; Accepted 24 February 2024
Available online 25 February 2024

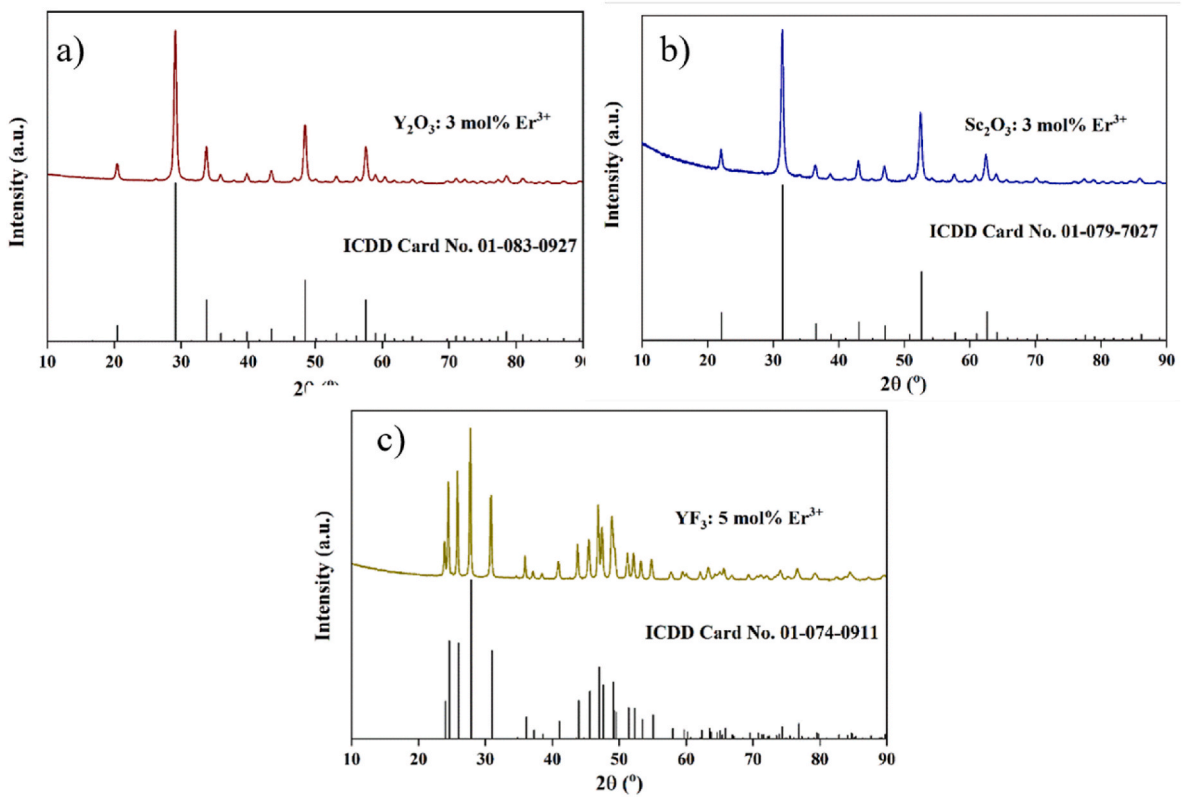

Fig. 1. XRD pattern of Er^{3+} doped: a) Y_2O_3 with corresponding ICDD card No. 01-083-0927, crystallite size = 17 nm; b) Sc_2O_3 with corresponding ICDD card No. 01-079-7027, crystallite size = 13 nm and c) YF_3 with corresponding ICDD card No. 01-074-0911, crystallite size = 34 nm.

Sc_2O_3 fluorescence has been studied in its ceramic form for the creation of eye safe lasers, exploiting the 1.5 μm emission. In its nanoparticle form however, it has been investigated as a possible oxide material for biological applications [13].

On the other hand, fluoride nanoparticles have been proposed for their excellent upconversion properties and Er:YF_3 has been investigated for spectral conversion in photovoltaics [14,15].

In this work we present a comparison of the multicolor emission of both sesquioxide and fluoride nanoparticles doped with Er ions. All samples show a very wide emission spectral range from visible to mid infrared around 2.8 μm with a non-trivial relative intensity behaviour. Furthermore, the emission cross sections of the infrared transitions have been calculated and compared with the literature for the oxide samples providing a confirmation of the published values for the near infrared emission, a correction for the mid-infrared emission of Er:Y_2O_3 and new results for the Er:Sc_2O_3 sample. Moreover, the 1.5 μm infrared emission has been exploited for in-band LIR thermometry applications in the physiological temperature range, i.e. from approximately 18 °C to 45 °C and a comparison of the results within the three compounds and with the literature is presented.

2. Materials and methods

2.1. Chemicals and materials

The following chemicals: yttrium oxide- Y_2O_3 (Alfa Aeser, 99.9%), erbium oxide- Er_2O_3 (Alfa Aeser, 99.99%), scandium oxide- Sc_2O_3 (Alfa Aeser, 99.9%), polyethylene glycol- PEG 200 (Alfa Aesar), nitric acid- HNO_3 (Macron, 65%) and ammonium hydrogen difluoride- NH_4HF_2 (Sigma Aldrich, 98.5%) were purchased and used as received.

2.2. Synthesis of the nanoparticles

The YF_3 samples doped with 5 mol% Er^{3+} ($Y_{0.95}Er_{0.05}F_3$) and 10 mol % Yb^{3+}/5 mol% Er^{3+} ($Y_{0.85}Yb_{0.1}Er_{0.05}F_3$) have been synthesized from the appropriate quantities of Y_2O_3, Er_2O_3 and Yb_2O_3 which were mixed with NH_4HF_2 and grounded in an agate mortar and then heated, first in the air at 170 °C for 20 h and then at 500 °C for 3 h in a reducing atmosphere (Ar-10% H_2). The Y_2O_3 and Sc_2O_3 samples doped with 3 mol% Er^{3+} ($Y_{1.94}Er_{0.06}O_2$ and $Sc_{1.94}Er_{0.06}O_3$) and 10 mol% Yb^{3+}/3 mol% Er^{3+} were synthesized using the combustion method [16]. In the first step, appropriate amounts of oxides were dissolved in hot nitric acid under continuous stirring (130 °C), followed by the addition of PEG 200 as a fuel and chelating agent (mass ratio 1:1). The obtained solution was stirred at 80 °C until complete evaporation and formation of a clear gel. A voluminous white powder is produced when the gel is pre-sintered in a ceramic crucible at 800 °C for 2 h. The powder was then formed into pellets, which were calcinated at 1100 °C for 24 h.

Crystal structures of the powders were studied with an X-ray diffractometer (XRD) from Rigaku SmartLab (Cu-$K_{\alpha1,2}$ radiation, λ = 0.1540 nm) at room temperature. All measurements were recorded over the 2θ range of 10°–90°, with a step size of 0.01° and a counting time of 1°/min. The morphology of the prepared sample was defined by a field emission gun TESCAN MIRA3 scanning electron microscope (SEM). The samples were coated with a thin layer of Au using a typical sputtering technique (Polaron SC502 - Fison Instruments, UK).

For visible and infrared emissions, the samples were pumped with a 450 nm diode laser. The laser output power was between 60 and 100 mW depending on the sample. Visible emission was collected with a 5 cm focal length lens and sent to the input fiber of a compact spectrometer (AvaSpec-ULS2048L-SPU2, Avantes, Netherlands) with 1 nm resolution. For infrared measurements the emitted fluorescence was collected by a parabolic mirror and sent to a FTIR spectrometer (Magna860, Nicodom Ltd., Czech Republic) equipped with a MCT

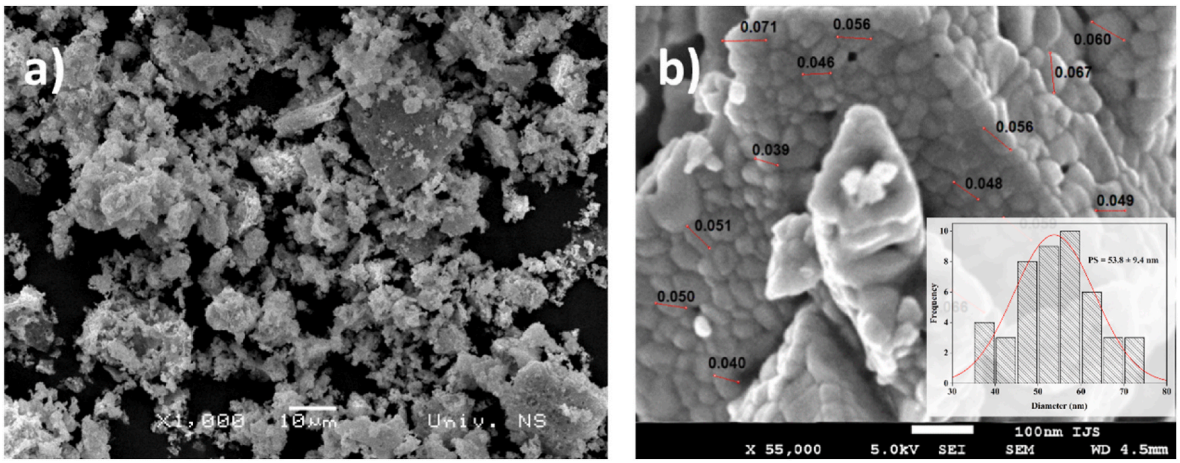

Fig. 2. Scanning electron microscopy images of a) representative Y_2O_3: Er^{3+} for combustion synthesis and b) YF_3: Er^{3+} sample with size distribution histogram given as inset.

cooled detector. Resolution of the emission measurements have been set to 1 cm^{-1} in the entire MIR range. Spectra have been corrected for the spectral response of the system using a blackbody source in the entire infrared region. In all cases, spectra are presented as a function of the variable with constant resolution (wavelength in nm for spectra acquired with the compact spectrometer and energy in cm^{-1} for those acquired with the FTIR spectrometer) with the other one reported as an upper axis for completeness.

For luminescence thermometry study, the doubly Yb,Er doped samples have been used. Samples have been pumped with a 980 nm diode laser, with output power between 90 and 130 mW and the emitted signal has been collected by a parabolic mirror and sent to the FTIR spectrometer, as before. The sample was placed in a thermally-isolated holder and the temperature was varied with a Peltier cell in the physiological range from approximately 15 °C–55 °C.

Emission cross-sections with data acquired using an FTIR spectrometer are calculated through the beta-tau method (also called Füchtbauer–Ladenburg) with the equation for fixed frequency intervals [17,18]:

$$\sigma_{em}(\nu) = \frac{c^2 I(\nu)}{8\pi\tau n^2 h\nu^3 \int \frac{I(\nu)}{h\nu} d\nu} \quad (1)$$

where $I(\nu)$ is the measured fluorescence signal, c, h, n and τ are the speed of light, the Plank's constant, the refractive index of the host matrix, taken at the wavelength that we are analysing, and the radiative lifetime of the level under consideration, respectively. One key point of this method is that the integral must be performed over the entire emission band of the upper level we are considering. For this reason, particular attention must be paid to acquire all the possible decay channels from the emitting level to all the lower ones, not just the transition under investigation. Moreover, all these possible emissions must be relatively calibrated to correct for possible different spectral responses of the acquisition system (optics, detectors …). In our case, we collected all the emissions with the same experimental setup (the FTIR spectrometer) to ensure identical experimental conditions and corrected the results for the spectral response of the system using a blackbody source.

3. Results

The XRD measurements presented in Fig. 1a and b confirm that both Er^{3+} doped Y_2O_3 and Sc_2O_3 samples crystallize in a cubic structure with the main diffraction peaks indexed according to the presented ICDD cards, No. 01-083-0927, and No. 01-079-7027, respectively. For Er^{3+} doped YF_3, all the diffraction reflections can be indexed in a single-phase orthorhombic β-YF_3 structure type, ICDD card No. 01-074-0911

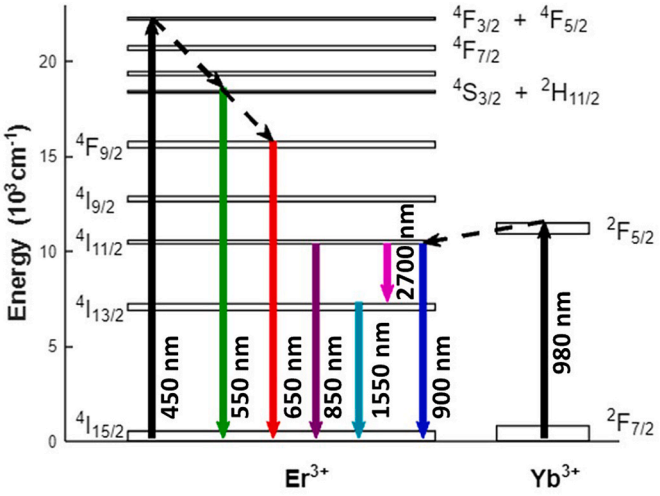

Fig. 3. Energy level scheme of Yb^{3+},Er^{3+} ions with all the observed transitions shown as arrows. The dotted arrows represent the non radiative transitions.

(Fig. 1c). No other phase peaks or traces of impurities were detected confirming the synthesis of a single-phase material and effective incorporation of both Er^{3+} ions into the cubic lattice. Also, the same valence and similar ionic radii of the Y^{3+}/Sc^{3+} and Er^{3+} ions indicate that it is possible to successfully incorporate the doping ions into the host materials [19]. Additionally, built-in PDXL2 software was used to calculate the average crystallite size given in Fig. 1 caption.

Scanning electron microscopy was carried out to investigate the morphology of the obtained powders; the micrographs of the representative Y_2O_3: Er^{3+} for combustion synthesis, and YF_3: Er^{3+} samples are presented in Fig. 2a and b, respectively. The Y_2O_3: Er^{3+} image (Fig. 2a) shows at the micron level flake-like, dense, and agglomerated particles, which seem to be less fluffy compared to particles obtained using the conventional combustion method and combustion agents other than PEG, as shown in our previous work [20]. The SEM image of the YF_3: Er^{3+} sample (Fig. 2b) shows agglomerated, irregularly shaped particles of approximately 54 nm in size on average (size distribution histogram is presented as an inset in Fig. 2b).

3.1. Visible spectroscopy

Erbium has a complex energy level scheme which can give rise to many emission channels. Fig. 3 shows the Dieke diagram of both Er and

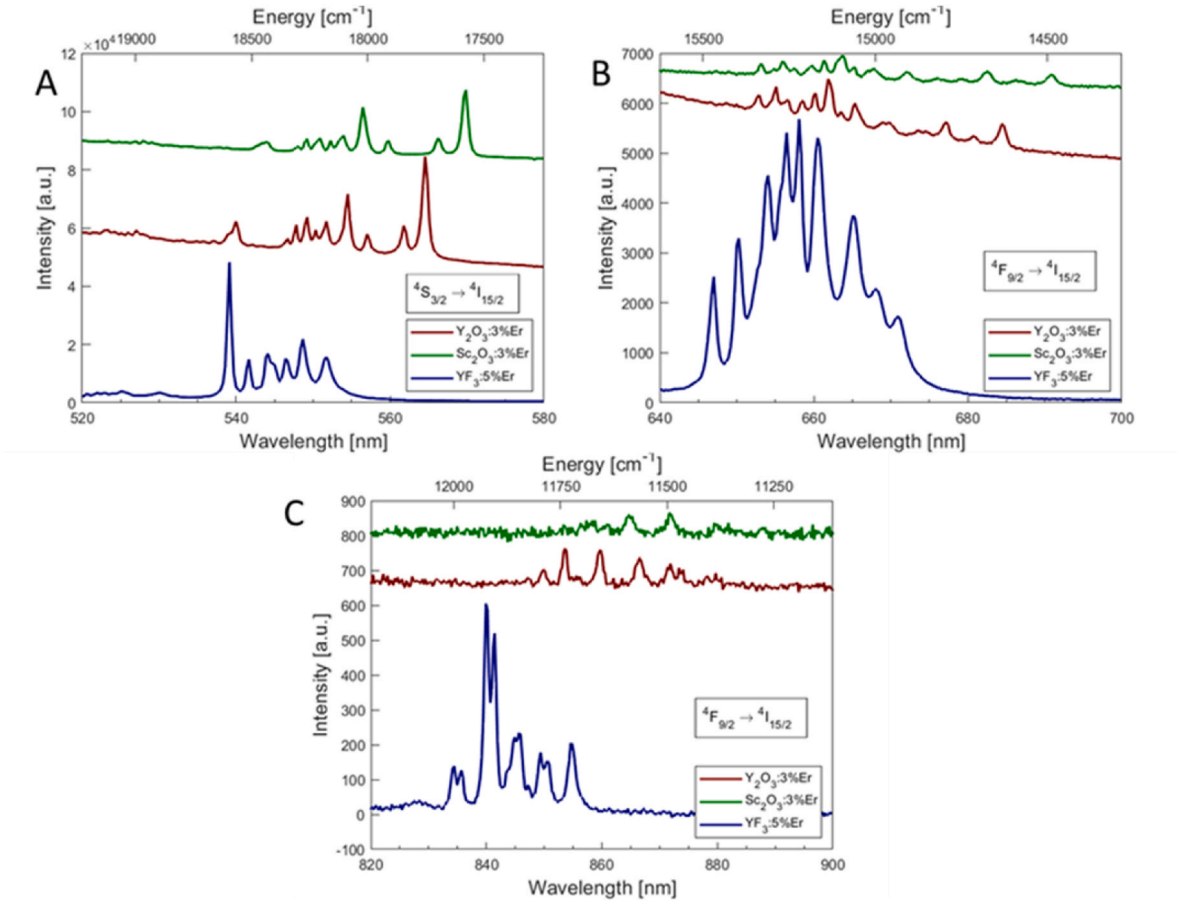

Fig. 4. A) Green emission from $^4S_{3/2} \rightarrow {}^4I_{15/2}$ transition of Er^{3+} ions; B) Red emission from the $^4F_{9/2} \rightarrow {}^4I_{15/2}$ transition of Er^{3+} ions; C) Near-infrared emission from the $^4I_{9/2} \rightarrow {}^4I_{15/2}$ transition of Er^{3+} ions.

Yb systems with all the emission bands we were able to observe both in the visible and infrared regions from the three compounds. For samples doped with Er, after pumping at 450 nm several cascaded non-radiative transitions populate the levels responsible for the visible emissions, i.e. $^4S_{3/2}$ and $^4F_{9/2}$ [21]. The samples doped with Yb,Er instead, were pumped with a 980 nm laser and the $^4F_{5/2}$ Yb level was populated. From there, an energy transfer process populates the $^4I_{11/2}$ level of the Er ions. From $^4I_{11/2}$ Er level, part of the radiation can be emitted radiatively, and part can non radiatively decay to the $^4I_{13/2}$ level that will then emit at around 1.5 μm [5].

Visible emission comes from the decay of two different multiplets ($^4S_{3/2}$ and $^4F_{9/2}$) to the ground state. These two emission bands emit in the green and red regions, respectively and have been identified using the Dieke diagram reported in Fig. 3.

3.1.1. $^4S_{3/2}$ emission

The green emission band from the three different compounds is reported in Fig. 4A. It corresponds to the $^4S_{3/2} \rightarrow {}^4I_{15/2}$ transition with a weak contribution from the $^2H_{11/2} \rightarrow {}^4I_{15/2}$ transition in the short-wavelength part of the spectrum. These two bands are usually exploited for luminescence thermometry in the visible range. In sesquioxides, it extends from 540 to 570 nm with a maximum in intensity located at the long wavelength side of this emission region. As expected from the effect of the strong crystal field on sesquioxide matrices [22], these samples present wide emission bands composed of separated peaks and the peaks of Er:Sc_2O_3 tend to be red-shifted with respect to Er:Y_2O_3. The Er:YF_3 sample, instead, shows a continuous band that extends in a much narrower interval, from 535 to 555 nm with a maximum in intensity located around 540 nm.

3.1.2. $^4F_{9/2}$ emission

The visible emission from $^4F_{9/2}$ is shown in Fig. 4B. It is located in the red region and corresponds to the $^4F_{9/2} \rightarrow {}^4I_{15/2}$ transition. In sesquioxides, it is composed by separated peaks and extends for over 40 nm from 650 to 695 nm with the maximum at around 665 nm. The fluoride sample shows a very intense band in this region composed of one single structure that extends from 640 to 680 nm and several peaks superimposed, the highest of which is around 660 nm.

For both visible emissions the two sesquioxide samples show very similar spectra. In fact, we can see that the peak position and relative intensity are almost identical due to the isomorphism of the two crystal matrices: Y_2O_3 and Sc_2O_3. The main difference between the two spectra is the absence of a few lines and a slight shift in the peak position due to the different crystal field strength in the two compounds [23]. Instead, the fluoride compound shows much broader spectra with less separated lines and completely different peak position and intensity.

3.2. Near and mid infrared spectroscopy

The NIR region is characterized by two emission bands corresponding to the decay of the $^4I_{9/2}$ and $^4I_{11/2}$ to the ground state at around 850 nm and 1 μm and are reported in Figs. 4C and 5A.

3.2.1. $^4I_{9/2}$ emission

The emission in Fig. 4C is assigned to the $^4I_{9/2} \rightarrow {}^4I_{15/2}$ transition. For all the three samples the fluorescence structure is composed by separated peaks. Sesquioxide emission extends from 850 to 875 nm with a maximum in intensity at around 855 and 870 nm for the Y_2O_3 and the Sc_2O_3 samples, respectively. The fluoride emission is much more

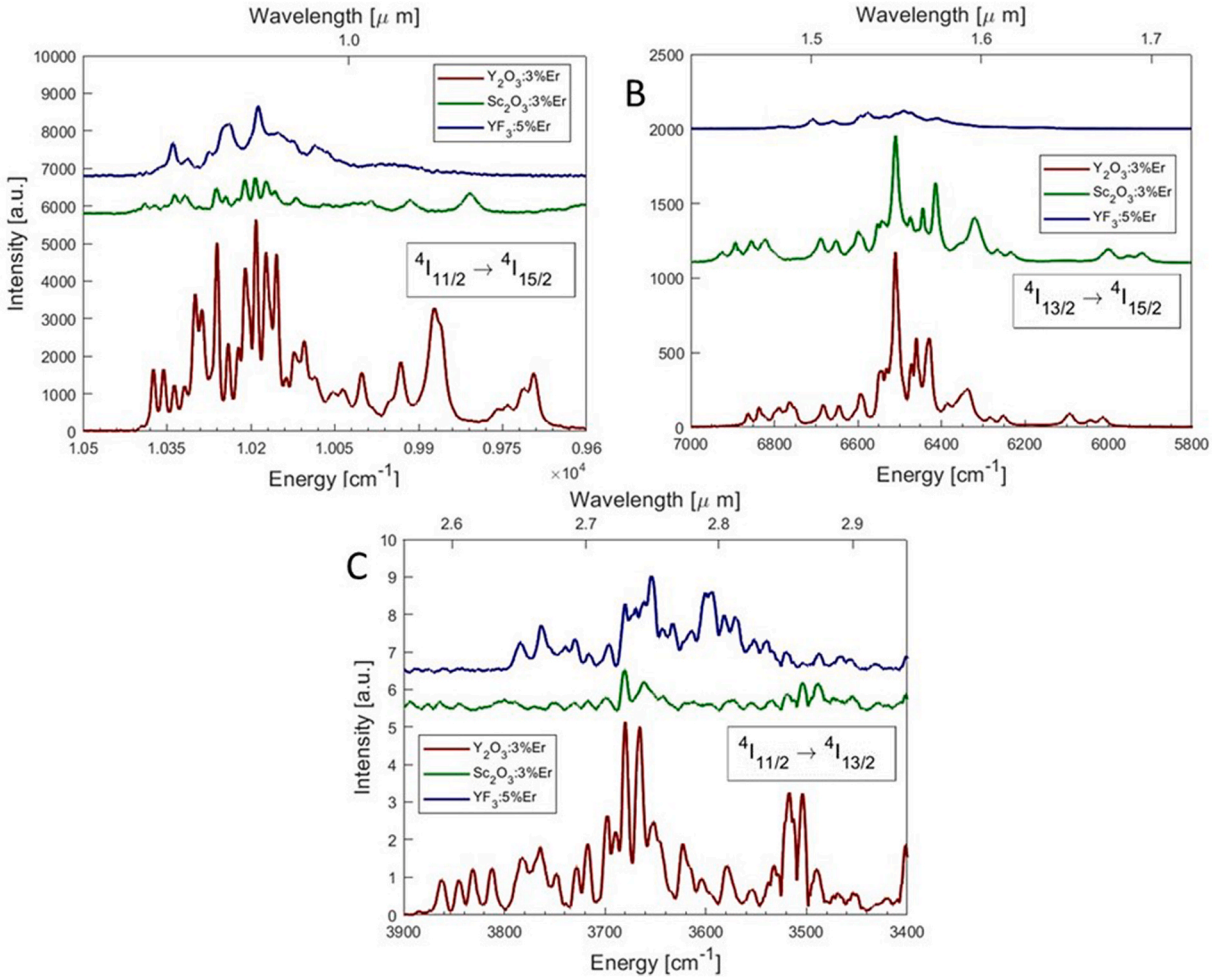

Fig. 5. A) Infrared emission from the $^4I_{11/2} \rightarrow {}^4I_{15/2}$ transition of Er^{3+} ions; B) Mid infrared emission from the $^4I_{13/2} \rightarrow {}^4I_{15/2}$ transition of Er^{3+} ions; C) Infrared emission from the $^4I_{11/2} \rightarrow {}^4I_{13/2}$ transition of Er^{3+} ions.

intense, it extends from 830 to 860 nm and presents a maximum at 840 nm.

3.2.2. $^4I_{11/2}$ emission

Fig. 5A shows the emission band corresponding to the $^4I_{11/2} \rightarrow {}^4I_{15/2}$ transition. In sesquioxides it appears as a series of well separated peaks and extends approximately from 10400 cm^{-1} to 9750 cm^{-1} (960 nm and 1026 nm, respectively) with a maximum located at around 10200 cm^{-1} (980 nm). In this region, the strongest emission is from the Er: Y_2O_3 sample. The fluoride sample, in this case, shows a weak broadband that extends from 10400 cm^{-1} to 10000 cm^{-1} (961 nm and 1 μm, respectively) with a maximum at 10190 cm^{-1} (981 nm).

The $^4I_{11/2}$ level has a second decay channel to the $^4I_{13/2}$ multiplet. Fig. 5C reports this second emission band that, as expected, is located around 2.7 μm. Given the large number of energy sublevels involved in the two multiplets (6 and 7 for $^4I_{11/2}$ and $^4I_{13/2}$, respectively) this band has a complicated structure that covers the 3500 - 3850 cm^{-1} (2.86–2.6 μm) region almost continuously in both sesquioxide samples. The total number of possible sublevel transitions is 42, and this explains the large number of peaks observed in this region. Although the measurement is taken at room temperature, all the peaks are very sharp, much sharper, for example, then those published by Ref. [24] in Y_2O_3 and this confirms the good spectroscopic quality of our samples. The strongest emission is from the Er: Y_2O_3 sample with a maximum located around 3700 cm^{-1} (2.7 μm). For Er:YF_3 the emission intensity is similar and the band is composed of many sharp peaks, but it extends from 3550 to 3800 cm^{-1} (2.81–2.63 μm) with two peaks with similar intensity at 3671 cm^{-1} and 3651 cm^{-1} (2.72 μm and 2.74 μm, respectively).

Table 1
Peak emission cross section of the transitions originating from the $^4I_{11/2}$ level.

Crystal	Transition	Peak (cm^{-1})	Peak (μm)	σ_{em} ($10^{-20}cm^2$) [this work]	Literature values [Ref]
Y_2O_3	$^4I_{11/2} \rightarrow {}^4I_{15/2}$	1019	0.981	0.6	
	$^4I_{11/2} \rightarrow {}^4I_{13/2}$	3689	2.71	0.7	
			2.723		1.41 [24]
			–		10 [27]
	$^4I_{13/2} \rightarrow {}^4I_{15/2}$	6511	1.536	1.76	1.55 [28]
		6092	1.641	0.20	0.178 [11]
		6014	1.663	0.16	0.147 [11]
Sc_2O_3	$^4I_{11/2} \rightarrow {}^4I_{15/2}$	1019	0.981	0.3	
	$^4I_{11/2} \rightarrow {}^4I_{13/2}$	3675	2.72	0.43	
	$^4I_{13/2} \rightarrow {}^4I_{15/2}$	6510	1.536	1.24	
			1.534		1.8 [26]
		6000	1.667	0.22	
		5920	1.689	0.17	

These two bands together originate from the decay of the $^4I_{9/2}$ multiplet to the two lower lying multiplets. Since we acquired the two emissions with the same experimental setup and we calibrated the

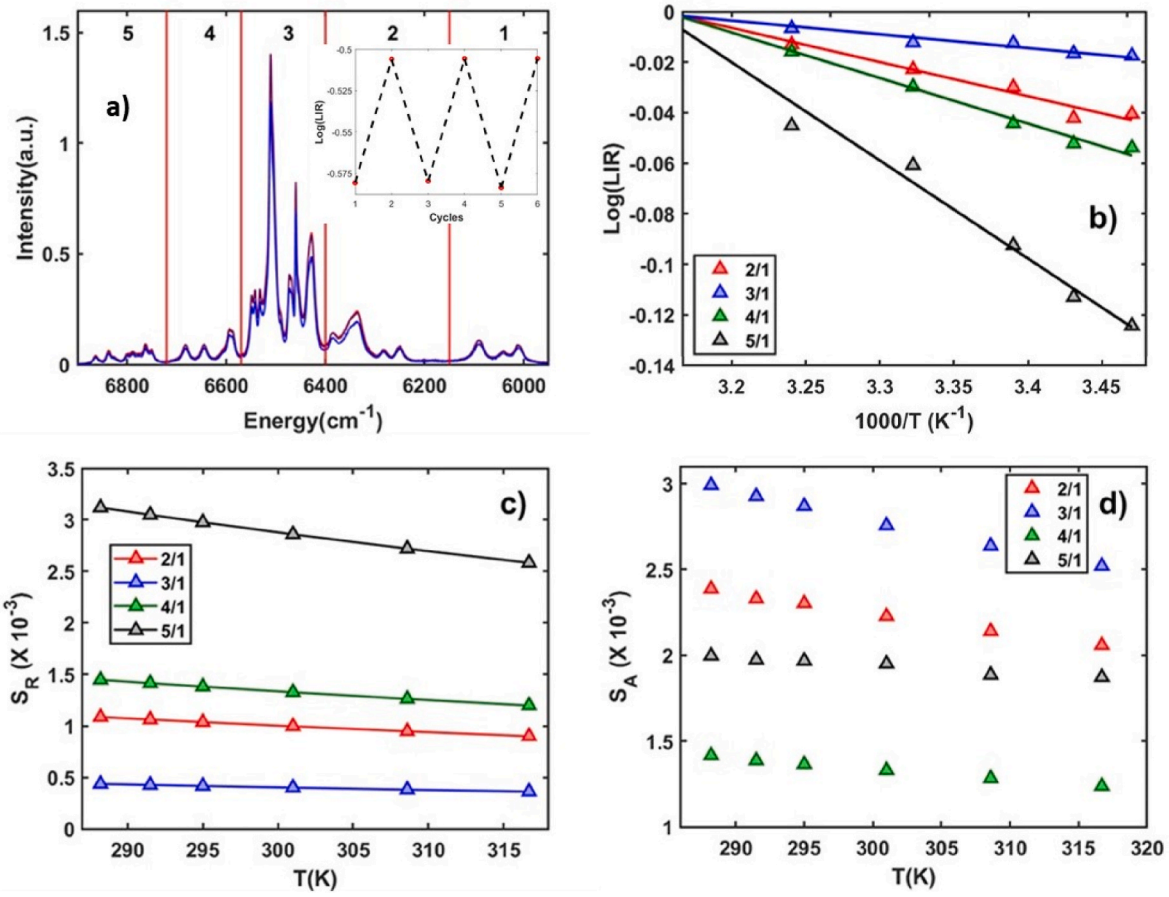

Fig. 6. a) Emission spectra of Yb,Er:Y_2O_3 nanoparticles as a function of the temperature with the boundaries between the various regions considered. The inset shows the stability of the levels that give the best S_R results, i.e. I_5/I_1; b) LIR of the various regions referred to region 5; c) Relative sensitivity of the same LIRs shown in a); d) Absolute sensitivity of the same LIRs shown in a).

response of the system with a blackbody source, we could use these emissions to calculate the emission cross sections of these two bands using eq. (1) including both bands in the integral at the denominator. To this aim, we took the refractive indexes from Ref. [25] (n = 1.9 for Y_2O_3 and n = 1.97 for Sc_2O_3) and the radiative lifetimes from the literature, when available. We could not measure the radiative lifetime because it corresponds to the experimental lifetime in absence of nonlinear and non-radiative decays. This means that it should be measured in low-concentration samples and taken at low temperature. Therefore, we relied on published values which are usually calculated with the Judd Ofelt theory in bulk crystals or ceramics. For Y_2O_3 we used $\tau = 3.43$ msec calculated by Hou and coworkers [24] in single crystals, and for Sc_2O_3 we used $\tau = 3.96$ msec calculated by Gheorge et al. [26] in glass ceramics. For the fluoride compound we could not find any proper reference in the literature, therefore, we could not perform the calculation. Results are reported in Table 1 together with the comparison with literature values. The highest emission cross section in the 2.7 μm region is obtained with Er:Y_2O_3. This compound shows a maximum at 3689 cm^{-1} (2.71 μm) with a value of 0.7 10^{-20} cm^2. This value is a factor of two lower than that reported by Ref. [24] and an order of magnitude lower than that calculated by Ref. [27], but it must be noted that these authors did not consider the $^4I_{11/2} \rightarrow {}^4I_{13/2}$ emission in the calculation, leading to an overestimation of the emission cross section value. Since our emission cross section value for the $^4I_{13/2} \rightarrow {}^4I_{15/2}$ transition, which is a single emission from the upper level, agrees with the literature, we propose our results as a correction over published values for the $^4I_{11/2} \rightarrow {}^4I_{13/2}$ and $^4I_{11/2} \rightarrow {}^4I_{15/2}$ transitions that start from the same level and must, therefore, be calculated as a single band with eq. (1). This means that both bands must be acquired with the same experimental setup and their intensity must be relatively calibrated with a black body source. After this procedure, the integral of both bands together must be used in the denominator of eq. (1) for the $^4I_{11/2} \rightarrow {}^4I_{13/2}$ and $^4I_{11/2} \rightarrow {}^4I_{15/2}$ emission cross section calculation. The maximum emission cross section values for Er:Sc_2O_3 at 3675 cm^{-1} (2.72 μm) is 0.42 10^{-20} cm^2. No literature results could be found for comparison with this compound.

In Table 1, we also report the maximum emission cross section of Er in both compounds for completeness.

3.2.3. $^4I_{13/2}$ emission

Lastly, we were able to detect the main infrared Erbium emission in the 1.5 μm region. This is reported in Fig. 5B. This emission band corresponds to the $^4I_{13/2} \rightarrow {}^4I_{15/2}$ transition and it extends from 5800 to 7000 cm^{-1} with a maximum around 6500 cm^{-1} for all the samples. Strangely, the highest emission intensity is reported for the two oxide compositions which show very similar spectra, even if the Er:Sc_2O_3 spectrum extends in a somewhat larger range. We calculated the emission cross section of this transition following the same procedure described above. For $^4I_{13/2}$ in Y_2O_3 we used the lifetime calculated by Ref. [24] and for Sc_2O_3 that calculated by Ref. [26]. These are 4.88 msec and 4.5 msec, respectively. We did not calculate the emission cross section for the fluoride compound because we could not find a proper reference for the radiative lifetime of this level. The maximum emission cross section for Er:Y_2O_3 is 1.76 10^{-20} cm^2 obtained at 6511 cm^{-1} (1.536 μm). This value is comparable with that obtained in Ref. [28] at nearly the same wavelength. Moreover, since this emission line is affected by reabsorption, emission peaks at longer wavelengths are usually reported. In this region, the maximum emission cross sections obtained are 0.196 10^{-20} cm^2 at 6092 cm^{-1} (1.641 μm) and 0.156 10^{-20}

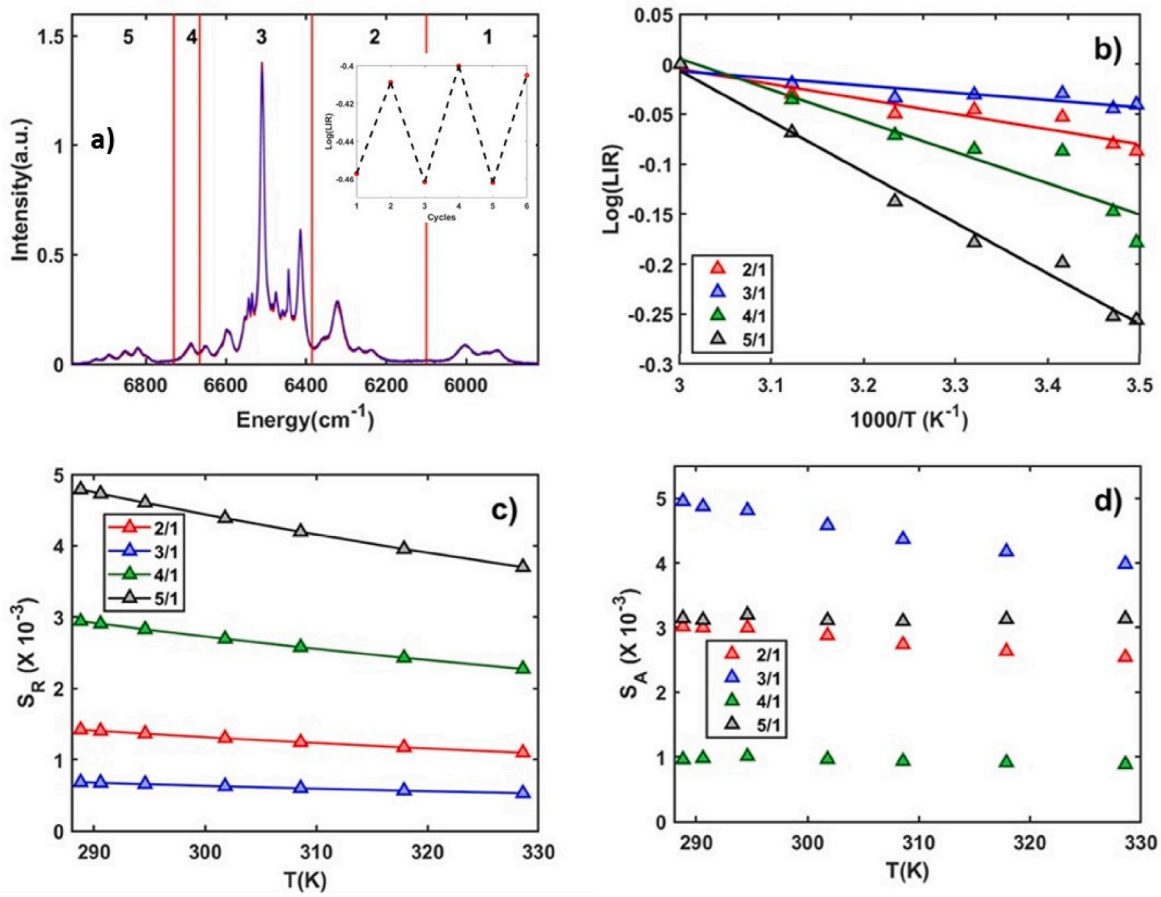

Fig. 7. a) Emission spectra of Yb,Er:Sc_2O_3 nanoparticles as a function of the temperature with the boundaries between the various regions considered. The inset shows the stability of the levels that give the best S_R results, i.e. I_5/I_1; b) LIR of the various regions referred to region 5; c) Relative sensitivity of the same LIRs shown in a); d) Absolute sensitivity of the same LIRs shown in a).

cm^2 at 6014 cm^{-1} (1.663 μm) in very good agreement with values calculated in Ref. [11] (0.178 10^{-20} cm^2 and 0.147 10^{-20} cm^2, respectively) at the same wavelengths. Er:Sc_2O_3 shows slightly lower emission cross sections; the maximum value is 1.24 10^{-20} cm^2 at 6092 cm^{-1} (1.641 μm) but the emission spectrum extends at longer wavelengths and the long wavelength maxima are 0.22 10^{-20} cm^2 at 6000 cm^{-1} (1.667 μm) at and 0.17 10^{-20} cm^2 at 5920 cm^{-1} (1.689 μm).

This emission has been used for luminescence thermometry in the third biological window, as detailed in the next section.

3.3. Luminescence thermometry on the $^4I_{13/2} \rightarrow {}^4I_{15/2}$ transition

The $^4I_{13/2} \rightarrow {}^4I_{15/2}$ emission spans for over 1000 cm^{-1} and lies almost completely in the third biological window, therefore it is a very interesting region for biological applications. For these reasons, we explored the possibility of using this transition for luminescence thermometry. Unlike the green emission usually used for luminescence thermometry with Er-doped compounds, this emission involves only sublevels from one single multiplet, therefore, there is no natural separation between emission from two different Er multiplets. This is why we divided the emission spectra into different regions and calculated the integral of the luminescence in each region. Secondly, we calculated the luminescence intensity ratio (LIR) from all possible combinations and varied the boundaries between the various regions to find the best conditions to maximize the LIR variation with temperature.

Assuming a Boltzmann distribution for the population of the various sublevels within the $^4I_{13/2}$ multiplet, LIR is expected to have an exponential dependence:

$$LIR = \frac{I_U}{I_L} = A\ exp\left(-\frac{\Delta E}{kT}\right) \tag{2}$$

with I_U and I_L are the integrals of the upper and lower region, respectively and ΔE connected to the energy distance between the regions used for I_U and I_L. LIR can be used to calculate the relative and absolute sensitivities which are vital parameter to assess the temperature sensing ability of the compound. The absolute sensitivity is defined as:

$$S_A = \frac{\delta(LIR)}{\delta T} = \frac{\Delta E}{kT^2} A\ exp\left(-\frac{\Delta E}{kT}\right) = \frac{\Delta E}{kT^2}\ LIR \tag{3}$$

The relative sensitivity is a measure of the extent of change of LIR following a change in temperature and is given by:

$$S_R = \frac{S_A}{LIR} = \frac{\Delta E}{kT^2} \tag{4}$$

We also studied the measurement uncertainty and the temperature resolution by cycling between two temperatures. The study follows the procedure reported in Refs. [29,30] that consists in calculating the LIR uncertainty (δLIR) as the standard deviation of the reproducibility measurements. We used this number to calculate the temperature uncertainty using the following equation:

$$\delta T = \frac{1}{S_r} \frac{\delta\ LIR}{LIR} \tag{5}$$

We perform this analysis for the best LIR result of each sample. The results are reported in the figures as an inset.

In the following, we show the best results obtained with each

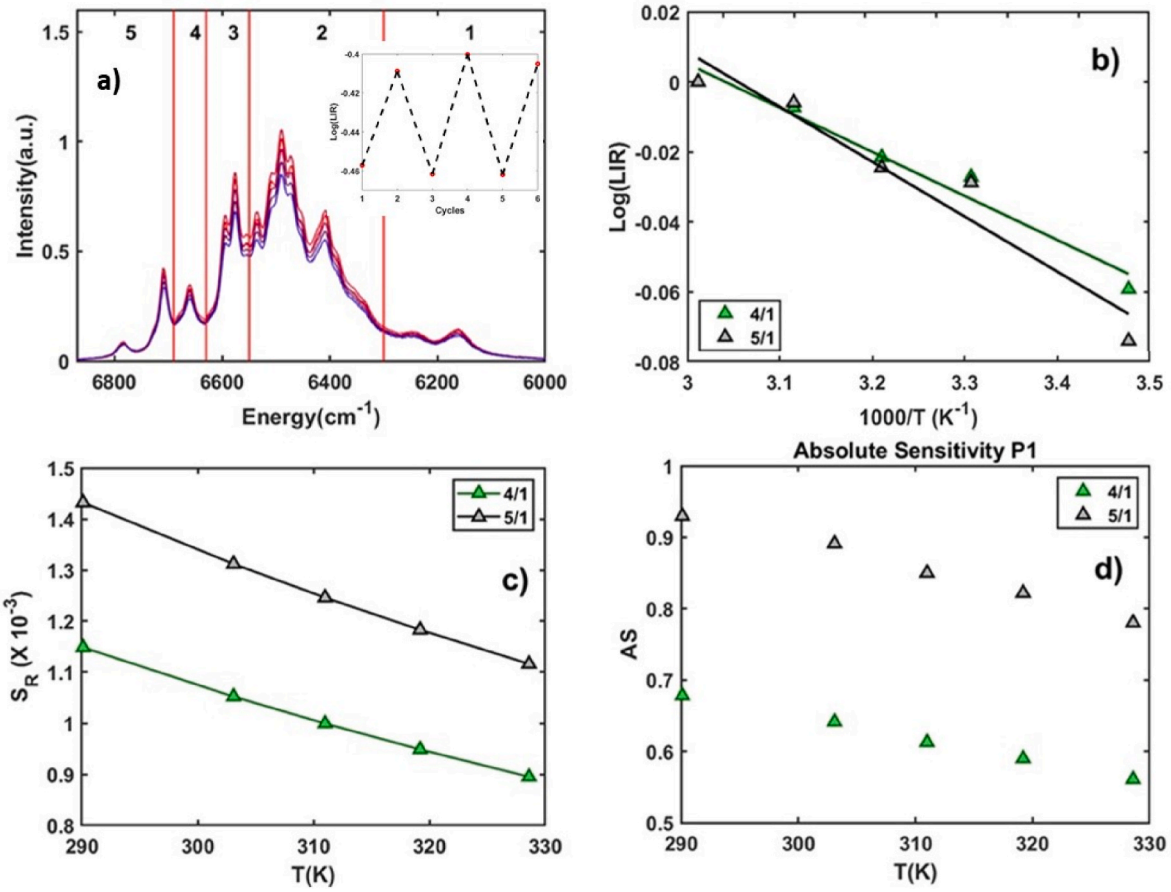

Fig. 8. a) Emission spectra of Yb,Er:YF_3 nanoparticles as a function of the temperature with the boundaries between the various regions considered. The inset shows the stability of the levels that give the best S_R results, i.e. I_5/I_1; b) Best LIR of the various regions referred to region 5; c) Relative sensitivity of the same LIRs shown in a); d) Absolute sensitivity of the same LIRs shown in a).

compound.

Fig. 6 shows the results obtained with Yb,Er:Y_2O_3 sample. As expected, the strongest temperature dependence of the LIR is obtained between the two extreme regions (1–5) of the spectrum. The maximum relative sensitivity is 3.1 10^{-3} at 288 K which decreases to 2.6 10^{-3} at 317 K. The absolute sensitivity shows a similar trend on all transitions, but the highest value is found for the 3-1 regions. This is because the maximum intensity of the emission is concentrated in the central part of the spectrum. Unfortunately, this feature is common to all investigated compounds. Anyway, the maximum absolute sensitivity for the 5-1 regions is 2 10^{-3} nearly constant in the whole investigated temperature range. We performed the reproducibility analysis on the ratio between those two regions obtaining an uncertainty of 0.1 °C at 40 °C and 0.7 °C at 20 °C.

Results obtained with Yb,Er:Sc_2O_3 sample are shown in Fig. 7. As for the previous compound, the strongest temperature dependence of the LIR is obtained between the two extreme regions (1–5) of the spectrum with a maximum relative sensitivity of 4.8 10^{-3} at 289 K which decreases to 3.7 10^{-3} at 329 K. Also in this case the highest intensity of the emission is concentrated in the central part of the spectrum, therefore the maximum absolute sensitivity is found for the 3-1 transition with a maximum value of 5 10^{-3}. The maximum absolute sensitivity for the 5-1 regions is 3.2 10^{-3} nearly constant in the whole investigated temperature range. We performed the reproducibility analysis on the ratio between those two regions obtaining an uncertainty of 0.6 °C at 40 °C and 1 °C at 20 °C.

The fluoride compound shows similar trends of the results if compared to the other compounds, but the absolute and relative sensitivities are in general lower. Results are shown in Fig. 8. Here we only show results relative to the 4-1 and 5-1 regions, as they are by far the best results obtained. The maximum relative sensitivity is 1.4 10^{-3} at 290 K and the maximum absolute sensitivity is 0.9 10^{-3} for the 5-1 region. The temperature uncertainty calculated from the cycling between

Table 2
Comparison of the LIR efficiency between different doping ions.

Material	Temperature range (K)	Transition	S_r[% K^{-1}]	Ref.
AlN:Nd^{3+}/Yb^{3+}	298–503	Nd:$^4F_{7/2} \rightarrow {}^4I_{9/2}$, Nd:$^4F_{5/2} \rightarrow {}^4I_{9/2}$	0.84 4.63	[33]
$LaPO_4$:Tm^{3+}/Yb^{3+}	293–773	Tm:$^3F_{2,3} \rightarrow {}^3H_6$ $^1D_2 \rightarrow {}^3F_4$	3.0	[34]
ScF_3:Yb^{3+}/Tm^{3+}	313–573	Tm: $^3F_{2,3} \rightarrow {}^3H_6$ $^1D_2 \rightarrow {}^3F_4$	1.60	[35]
$NaLuF_4$: Yb^{3+}/Ho^{3+}	390–780	Ho:$^5F_1$,$^5G_6$/$^5F_{2,3}$, $^3K_8 \rightarrow {}^5I_8$	0.83	[36]
YOF:Er^{3+}	298–523	$^4I_{13/2} \rightarrow {}^4I_{15/2}$	0.36	[4]
$BaMoO_4$:Er^{3+}/Yb^{3+}	293–553	$^4I_{13/2} \rightarrow {}^4I_{15/2}$	0.129	[5]
$LiErF_4$/$LiYF_4$ $LiErF_4$:Ce^{3+}/$LiYF_4$	293–318	$^4I_{13/2} \rightarrow {}^4I_{15/2}$	0.4 0.45	[6]
Y_2O_3:Yb^{3+}/Er^{3+}	288–317	$^4I_{13/2} \rightarrow {}^4I_{15/2}$	0.31	This work
Sc_2O_3:Yb^{3+}/Er^{3+}	289–329	$^4I_{13/2} \rightarrow {}^4I_{15/2}$	0.5	This work
YF_3:Yb^{3+}/Er^{3+}	290–329	$^4I_{13/2} \rightarrow {}^4I_{15/2}$	0.14	This work

20 °C and 40 °C is 1 °C at 20 °C and 0.8 °C at 40 °C.

As a result, the maximum relative sensitivity is of the order of 10^{-3} for all compounds which is slightly lower than typical values obtained in the visible region [31], and the best results are obtained with the two oxide compounds. Although unexpected, this result is in agreement with the finding that the best host materials are those where the energy difference between the two involve levels can be bridged by one or two phonons, whereas crystal hosts with lower phonon energy which require the involvement of more than two phonons are less efficient [32].

Moreover, we made a comparison with other works that use different doping ions in Table 2. Although some of the reported S_r values are higher than ours, they have been obtained from transitions in the visible or near infrared range. The last six lines of this table compare our results with those obtained with the same Er transition in published papers and our results compare well with those, with our result on Er:Sc_2Y_3 being the highest.

4. Conclusions

We carried out a spectroscopic investigation of three Er-doped nanoparticle compounds. Multicolor emission in an ultra-wide range from the visible (green) region to mid infrared (2.7 μm) has been observed. Emission cross-section values for near (1.5 μm) and mid infrared (2.7 μm) erbium emission in Er:Y_2O_3 and Er:Sc_2O_3 have been calculated and compared with literature results. Our results are in agreement with published values on Er:Y_2O_3 or constitute a correction for some of the published results.

The near infrared emission at around 1.5 μm in the three compounds have been used for luminescence thermometry in the third biological window. The maximum relative sensitivity obtained is 3.1 10^{-3} in Er:Y_2O_3.

CRediT authorship contribution statement

F. Gennari: Data curation, Formal analysis, Investigation, Methodology, Writing – original draft, Writing – review & editing. **J. Periša:** Formal analysis, Investigation, Visualization. **M. Sekulić:** Formal analysis, Investigation. **Ž. Antić:** Validation, Visualization, Writing – original draft. **M. Dramićanin:** Conceptualization, Methodology, Supervision. **A. Toncelli:** Conceptualization, Formal analysis, Methodology, Supervision, Validation, Writing – original draft, Writing – review & editing.

Declaration of competing interest

The authors declare that they have no known competing financial interests or personal relationships that could have appeared to influence the work reported in this paper.

Data availability

Data will be made available on request.

Acknowledgment

Authors from Vinča Institute would like to acknowledge funding of the Ministry of Science, Technological Development, and Innovation of the Republic of Serbia under contract 451-03-47/2023-01/200017.

References

[1] E.C. Ximendes, U. Rocha, T.O. Sales, N. Fernández, F. Sanz-Rodríguez, I.R. Martín, C. Jacinto, D. Jaque, In Vivo Subcutaneous thermal Video recording by Supersensitive infrared nanothermometers, Adv. Funct. Mater. 27 (2017) 1702249, https://doi.org/10.1002/adfm.201702249.

[2] Ł. Marciniak, A. Bednarkiewicz, M. Stefanski, R. Tomala, D. Hreniak, W. Strek, Near infrared absorbing near infrared emitting highly-sensitive luminescent nanothermometer based on Nd^{3+} to Yb^{3+} energy transfer, Phys. Chem. Chem. Phys. 17 (2015) 24315, https://doi.org/10.1039/c5cp03861h.

[3] I. Porosnicu, C. Colbea, F. Baiasu, M. Lungu, M. Cosmin Istrate, D. Avram, C. Tiseanu, A sensitive near infrared to near-infrared luminescence nanothermometer based on triple doped Ln-Y_2O_3, Methods Appl. Fluoresc. 8 (2020) 035005, https://doi.org/10.1088/2050-6120/ab8c20.

[4] N. Rakov, F. Matias, G.S. Maciel, M. Xiao, The near-infrared emission of Er^{3+}-doped yttrium oxy-fluoride ceramic powders: temperature reading using uncoupled and thermally coupled energy levels, J. Lumin. 263 (2023) 119991, https://doi.org/10.1016/j.jlumin.2023.119991.

[5] R. Lei, X. Liu, F. Huang, D. Deng, S. Zhao, H. Xu, S. Xu, Optical thermometry based on anomalous temperature-dependent 1.53 μm infrared luminescence of Er3+ in BaMoO4: Er3+/Yb3+ phosphor, Opt. Mater. 86 (2018) 278–285, https://doi.org/10.1016/j.optmat.2018.10.024.

[6] C. Hazra, A. Skripka, S.J.L. Ribeiro, F. Vetrone, Erbium single-band nanothermometry in the third biological imaging window: potential and Limitations, Adv. Opt. Mater. 8 (2020) 2001178, https://doi.org/10.1002/adom.202001178.

[7] A. Toncelli, J. Xu, A. Tredicucci, A.M. Heuer, C. Kränkel, Mid-infrared spectroscopic characterization of Pr^{3+} :Lu_2O_3, Opt. Mater. Express 9 (11) (Nov. 2019) 4464, https://doi.org/10.1364/OME.9.004464.

[8] F. Cornacchia, A. Toncelli, M. Tonelli, 2-μm lasers with fluoride crystals: Research and development, Prog. Quant. Electron. 33 (2–4) (Mar. 2009) 61–109, https://doi.org/10.1016/j.pquantelec.2009.04.001.

[9] C. Bouzigues, T. Gacoin, A. Alexandrou, Biological applications of Rare-Earth based nanoparticles, ACS Nano 5 (11) (Nov. 2011) 8488–8505, https://doi.org/10.1021/nn202378b.

[10] A.Q. Le Quang, J. Zyss, I. Ledoux, V.G. Truong, A.-M. Jurdyc, B. Jacquier, D.H. Le, e A. Gibaud, An Hybrid organic–inorganic approach to erbium-functionalized Nanodots for emission in the Telecom window, Chem. Phys. 318 (2005) 33–43, https://doi.org/10.1016/j.chemphys.2005.08.031.

[11] Ei E. Brown, U. Hömmerich, A. Bluiett, C. Kucera, J. Ballato, S. Trivedi, Near-infrared and upconversion luminescence in Er:Y_2O_3 ceramics under 1.5 μm excitation, J. Am. Ceram. Soc. 97 (2014) 2105–2110, https://doi.org/10.1111/jace.12898.

[12] Z. Qin, G. Xie, J. Zhang, J. Ma, P. Yuan, L. Qian, Continuous-wave and passively Q-switched Er:Y_2O_3 ceramic laser at 2.7 μm, International Journal of Optics 2018 (2018) 1–5, https://doi.org/10.1155/2018/3153614.

[13] H. Qin, J. Li, M. Yuan, Y. Peng, Y. Huang, C. Li, Solvothermal synthesis and upconversion luminescence of ultra-small Sc2O3: Yb, Er nanoparticles, Opt. Mater. 112 (2021) 110786, https://doi.org/10.1016/j.optmat.2020.110786.

[14] Jose Marques-Hueso, Daqin Chen, K. Sean, W. MacDougall, Yuansheng Wang, e Bryce S. Richards, Advances in spectral conversion for photovoltaics: up-converting Er $^{3+}$ doped YF 3 nano-crystals in transparent glass ceramic». a cura di Loucas Tsakalakos, California, San Diego, 2011, https://doi.org/10.1117/12.897526, 811102.

[15] A. Skuta, E. Talik, L. Lipińska, M. Michalska, A. Guzik, P. Zajdel, Investigations of YF3: 1% Er nanocrystals, J. Cryst. Growth 401 (Sep. 2014) 480–483, https://doi.org/10.1016/j.jcrysgro.2014.02.009.

[16] R.M. Krsmanović, Ž. Antić, M.G. Nikolić, M. Mitrić, M.D. Dramićanin, Preparation of Y_2O_3:Eu^{3+} nanopowders via polymer complex solution method and luminescence properties of the sintered ceramics, Ceram. Int. 2 (2011) 525–531.

[17] B. Aull, H.P. Jenssen, Vibronic interactions in Nd:YAG resulting in nonreciprocity of absorption and stimulated emission cross sections, IEEE J. Quant. Electron. 18 (1982) 925–930, https://doi.org/10.1109/JQE.1982.1071611.

[18] F. Gennari, M. Sekulić, T. Barudžija, Ž. Antić, M.D. Dramićanin, A. Toncelli, Infrared Photoluminescence of Nd-doped sesquioxide and fluoride nanocrystals: a comparative study, Crystals 12 (8) (Jul. 2022) 1071, https://doi.org/10.3390/cryst12081071.

[19] R.D. Shannon, Revised effective ionic radii and systematic studies of interatomic distances in halides and chalcogenides, Acta Crystallogr. A 32 (1976) 751–767, https://doi.org/10.1107/S0567739476001551.

[20] R.M. Krsmanović Whiffen, Ž. Antić, A. Speghini, M.G. Brik, B. Bártová, M. Bettinelli, M.D. Dramićanin, Structural and spectroscopic studies of Eu^{3+} doped Lu_2O_3-Gd_2O_3 solid solution, Opt. Mater. 36 (2014) 1083–1091, https://doi.org/10.1016/j.optmat.2014.01.039.

[21] N. Bednarska-Adam, M. Kuwik, T. Goryczka, B. Macalik, W.A. Pisarski, J. Pisarska, Down- and up-conversion luminescence processes in olivine-type ceramic phosphors Li_2AGeO_4:Er^{3+} (A = Zn, Mg), Opt. Mater. 143 (2023) 114301, https://doi.org/10.1016/j.optmat.2023.114301.

[22] P. von Brunn, A.M. Heuer, L. Fornasiero, G. Huber, C. Kränkel, Efficient laser operation of Nd^{3+}:Lu_2O_3 at various wavelengths between 917 nm and 1463 nm, Laser Phys. 26 (8) (Aug. 2016) 084003, https://doi.org/10.1088/1054-660X/26/8/084003.

[23] L. Hao, K. Wu, H. Cong, H. Yu, H. Zhang, Z. Wang, J. Wang, Spectroscopy and laser performance of Nd:Lu_2O_3 crystal, Opt Express 19 (2011) 17774.

[24] W. Hou, Z. Xu, H. Zhao, Y. Xue, Q. Wang, X. Xu, J. Xu, Spectroscopic analysis of Er: Y2O3 crystal at 2.7 Mm mid-IR laser, Opt. Mater. 107 (2020) 110017, https://doi.org/10.1016/j.optmat.2020.110017.

[25] https://refractiveindex.info.

[26] C. Gheorghe, S. Georgescu, V. Lupei, A. Lupei, e A. Ikesue, Absorption intensities and emission cross section of Er3+ in Sc2O3 transparent ceramics, J. Appl. Phys. 103 (2008) 083116, https://doi.org/10.1063/1.2903155.

[27] T. Sanamyan, J. Simmons, e M. Dubinskii, Efficient Cryo-cooled 2.7-μm Er3+-doped Y2O3 ceramic laser diode-pumped at 974 nm, in: *Conference on Lasers and*

Electro-Optics 2010, CMDD6, OSA, San Jose, California, 2010, https://doi.org/10.1364/CLEO.2010.CMDD6.

[28] D.K. Sardar, K.L. Nash, R.M. Yow, J.B. Gruber, Absorption intensities and emission cross section of intermanifold transition of Er^{3+} in Er^{3+}:Y_2O_3 nanocrystals, J. Appl. Phys. 101 (11) (Jun. 2007) 113115, https://doi.org/10.1063/1.2739301.

[29] M. Quintanilla, L.M. Liz-Marzán, Guiding Rules for selecting a nanothermometer, Nano Today 19 (2018) 126–145, https://doi.org/10.1016/j.nantod.2018.02.012.

[30] S. Balabhadra, M.L. Debasu, C.D.S. Brites, L.A.O. Nunes, O.L. Malta, J. Rocha, M. Bettinelli, L.D. Carlos, Boosting the sensitivity of Nd^{3+}-based luminescent nanothermometers, Nanoscale 7 (2015) 17261–17267, https://doi.org/10.1039/C5NR05631D.

[31] A. Ćirić, T. Gavrilović, M.D. Dramićanin, Luminescence intensity ratio thermometry with Er^{3+}: performance overview, Crystals 11 (2) (Feb. 2021) 189, https://doi.org/10.3390/cryst11020189.

[32] M. Suta, A. Meijerink, A Theoretical framework for ratiometric single ion luminescent thermometers—Thermodynamic and Kinetic Guidelines for optimized performance, Adv. Theory Simul. 3 (12) (Dec. 2020) 2000176, https://doi.org/10.1002/adts.202000176.

[33] J. Wang, X. Ding, T. Gao, H. Zheng, X. Wang, Q. Wang, C. Liu, Rectangular cross-sectional Nd^{3+}/Yb^{3+} co-doped AlN nanorods with strong up-conversion emission for high-sensitivity optical thermometry, J. Alloys Compd. 970 (2024) 172637, https://doi.org/10.1016/j.jallcom.2023.172637.

[34] M. Runowski, A. Shyichuk, A. Tyminski, T. Grzyb, V. Lavín, S. Lis, Multifunctional optical sensors for nanomanometry and nanothermometry: high-pressure and hightemperature upconversion luminescence of lanthanide-doped phosphates-LaPO4/YPO4:Yb^{3+}-Tm^{3+}, ACS Appl. Mater. Interfaces 10 (2018) 17269–17279, https://doi.org/10.1021/acsami.8b02853.

[35] M. Dai, Y. Li, Z. Wang, A. Li, T. Sheng, H. Xu, K. Li, Z. Fu, Thermally boosted upconversion luminescence and high-performance thermometry in ScF3:Yb3+/Tm3+ nanorods with negative thermal expansion, J. Lumin. 265 (2024) 120219, https://doi.org/10.1016/j.jlumin.2023.120219.

[36] S. Zhou, S. Jiang, X. Wei, Y. Chen, C. Duan, M. Yin, Optical thermometry based on upconversion luminescence in Yb^{3+}/Ho^{3+} co-doped $NaLuF_4$, J. Alloys Compd. 588 (2014) 654–657, https://doi.org/10.1016/j.jallcom.2013.11.132.